ORIGINAL ARTICLE

Design of a High Precision Multichannel 3D Bioprinter

Jintao Li[1], Bin Zhang[1*] , Yichen Luo[1] and Huayong Yang[1]

Abstract

Three-dimensional (3D) printing technology is expected to solve the organ shortage problem. However, owing to the accuracy limitations, it is difficult for the current bioprinting technology to achieve an accurate control of the spatial position and distribution of a single cell or single component droplet. In this study, to accurately achieve the directional deposition of different cells and biological materials in the spatial position for the construction of large transplantable tissues and organs, a high-precision multichannel 3D bioprinter with submicron-level motion accuracy is designed, and concurrent and synergistic printing methods are proposed. Based on the high-precision motion characteristics of the gantry structure and the requirements of concurrent and synergistic printing, a 3D bioprinting system with a set of 6 channels is designed to achieve six-in-one printing. Based on the Visual C++ environment, a control system software that integrates the programmable multi-axis controller (PMAC) motion, pneumatic, and temperature control subsystems was developed and designed. Finally, based on measurements and experiments, the 3D bioprinter and its control system was verified to fulfil the requirements of multichannel, concurrent, and synergistic printing with submicron-level motion accuracy, significantly shortening the printing time and improving the printing efficiency. This study not only provides an equipment basis for printing complex heterogeneous tissue structures, but also improves the flexibility and functionality of bioprinting, and ultimately makes the construction of complex multicellular tissues or organs possible.

Keywords 3D bioprinting, High precision, Concurrent and synergistic printing, Multichannel, Control system, Six-in-one printing

1 Introduction

3D printing is usually referred to as additive manufacturing (AM), which can rapidly produce parts with complex geometries that are labor-intensive or unachievable by traditional manufacturing methods [1]. This concept was presented in the 1980s and is widely used by enthusiasts and related industries [2]. Traditional 3D printing technology began with fused deposition modeling (FDM) in thermoplastics and the stereo lithography appearance (SLA) in photosensitive polymers [3]. However, several new printing methods, as well as equipment, have been developed to accommodate more materials such as metals [4–6], conductive inks [7–10], functional polymers [11–15], ceramics, and biocompatible hydrogels [16–18].

The 3D printing of multiple materials is considered. With the development of 3D printing, the technology of multi-material collaborative printing in the one-printing process is urgently needed. Studies have shown that the properties of products can be enhanced via multi-material printing, such as controllable material anisotropy, which is important for the manufacturing of functional devices or human tissues and organs [19]. Research regarding multi-material printing through the integration of printing technology has recently emerged. In 2003, Yan et al. [20] studied the use of a multi printhead 3D printing system in tissue engineering scaffolds of biomaterials

*Correspondence:
Bin Zhang
zbzju@163.com
[1] State Key Laboratory of Fluid Power Transmission and Control, School of Mechanical Engineering, Zhejiang University, Hangzhou 310027, China

Li *et al. Chinese Journal of Mechanical Engineering*   (2023) 36:140

Page 2 of 20

with a low viscosity. In 2005, Geng et al. [21] conducted an experiment to simultaneously distribute chitosan and NaOH using a robotic system. In addition, in 2014, Espalin et al. [22] studied the processing of multi-material structures using two legacy FDM machines. In 2016, Ding et al. [23] printed digital material structures with time-varying characteristics by combining materials with extensive mechanical properties and high-resolution printing technology using the self-assembly direct 4D printing method. Notably, the 3D-Bioplotter printer developed by envisionTEC can simultaneously print various biomaterials and control up to five different materials [24]. In addition, poly jet technology uses multiple inkjet printheads to spray different photosensitive polymer inks, which can produce structures composed of different materials.

As an emerging printing technology that aims to provide 3D printing scalability by enabling multiple 3D printers or printheads to collaborate at one-printing-process, collaborative 3D printing may reduce the manufacturing time, which is crucial to the development of scale-up technology [25]. However, studies regarding this new technology are currently limited. First, a complex control system responsible for coordinating and monitoring multiple devices is required. Second, reasonable print task allocation and avoidance of mutual collisions are difficult in the real-time printing process. Finally, the motion accuracy must be sufficiently high to ensure that the areas printed by the different robots are perfectly aligned. Research shows that a scalable 3D printing system composed of multiple cooperative manipulators provides a new idea for the development of large-scale 3D printing in the future [26, 27].

In 2014, Neri et al. [28] applied the robotic swarm-printing method to a large-scale construction industry. In that same year, the spider robot SiSpis of Siemens was able to perform 3D collaborative printing according to commands. Based on this strategy, Hunt et al. proposed the assumption that 3D printing with flying robots can facilitate collaborative 3D printing [29, 30]. In 2017, a method for simultaneously printing different parts of objects using multiple independent printheads was proposed in Autodesk's project Escher, as well as certain concepts created for the multi-printhead 3D printing machine [31–33]. In 2018, a solution that uses two mobile robots to print large concrete structures with synchronous positioning and mapping (SLAM) technology was proposed by the Nanyang Technological University (NTU) [34]. In that same year, AMBOTS developed a mobile robot team with special functions to enable them to automatically coordinate 3D printing tasks [35].

In 2017, Khani et al. [36] proposed a new hybrid layered multi-material bioprinting technology by combining a path planning and optimization algorithm with a multi-material hydrogel and biodegradable polymer dispensing system. In 2019, Joyee et al. [37] proposed a fully 3D printed, monolithic soft robot capable of linear and turning locomotion. This multi-modal, multi-material soft robot has a compliant body structure composed of magnetic particle-polymer composites and can be 3D printed directly from a digital computer model. In that same year, Roach et al. [1] proposed a new multi-material method (M^4) for a 3D printer composed of a variety of additive manufacturing technologies such as inkjet, fuse manufacturing, direct ink writing, and aerosol spraying, as well as a mechanical arm and light-curing module, which provides a wide range of functions for devices. Later that same year, Shen et al. [26] proposed a large-scale 3D printing system composed of multiple robots that work together. The results showed that the printing efficiency was improved by more than 73% compared to that of the conventional printing method. In 2022, Zhang et al. [27] overcame the limitations of conventional bioprinting systems by converting a six-degree-of-freedom robotic arm into a bioprinter, thereby enabling cell printing on 3D complex-shaped vascular scaffolds from all directions.

To accurately build transplantable organs or tissues with complex structures and diverse materials, the 3D printing platform is required to be multichannel, collaborative, synchronous, among other characteristics. However, studies have demonstrated that cooperative printing can be achieved by using a combination of multiple robots, and its motion precision is often at the millimeter level, which cannot satisfy the accurate control of the spatial position and distribution of a single cell or micro-sized droplets with a single component. Considering envisionTEC as an example, the printhead must be moved to a new point each time the material is changed, and the tool is then changed by vacuum adsorption. Thus, problems such as the time required, which may be significant, and the positioning accuracy cannot be guaranteed. To solve these problems, it is important to develop a printing system with a high degree of freedom and multiple printheads working synchronously. Accordingly, a multichannel 3D bioprinting platform with 18 motion degrees of freedom was developed in this study to conduct concurrent and synergistic printing. By developing a control program for the multichannel bioprinting platform, including motion, pneumatic, and temperature subsystem controls, the cooperative work of the subsystems of the printing platform was achieved. Both printing times are significantly shortened, and the

printing efficiency is improved. Note, the motion accuracy of the printer was controlled at the submicron level. A variety of biomaterials and non-biomaterials can be printed synchronously, which makes the construction of complex multicellular tissues and organs possible, and significantly improves the flexibility and functionality of bioprinting. This will provide an equipment basis for printing heterogeneous tissues and organs containing multiple cells and hardware support for the construction of organ tissues in vitro.

2 Design Principle of the High Precision Multichannel 3D Bioprinter

Currently, several types of 3D printing techniques are widely used. The principle of the multichannel 3D bioprinting platform designed in this study is based on FDM [38]. The multichannel feature was achieved using six printheads. Printable materials, which include not only biomaterials but also non-biomaterials, can be used in each printhead. Biomaterials include natural polymers, such as collagen, silk fiber, gelatin, alginate, or a mixture of the aforementioned. Non-biomaterials include the following synthetic polymers: thermoplastic hard materials such as polyethylene glycol (PEG), polylactic acid (PLA), and flexible materials.

3 Structural Design of High Precision Multichannel 3D Bioprinter

3.1 Design of Motion System

The 3D structure of the printer is shown in Figure 1. With two marble gantry frames, the stage has a high smoothness and stiffness, which meets the requirements of sports performance.

With 18 degrees of freedom, it can drive six printing printheads with a high precision and reliability. There are two marble gantry frames, one of which is fixed and the other is moving along the linear slide rail paved on the platform. The spatial motion is achieved by the movement of the marble gantry driven by the motor on the guide rail, including two X-axis guide rails, six Y-axis guide rails, and six Z-axis guide rails, which provide sufficient degrees of freedom for the printing equipment to achieve independent spatial translation. The forming size of this multichannel 3D bioprinter was designed to be 600 mm × 300 mm × 200 mm. The six X-Y motion stages have the same large working envelope of 0.6 m × 0.3 m, a local accuracy of ± 1 μm, repeatability of ± 0.6 μm, and a maximum velocity of 300 counts/msec (c/ms, 46.875 mm/s). The six Z-axis motion stages achieve a layer-by-layer deposition. Each Z-axis has 0.2 m of vertical travel, an accuracy of ± 1 μm, a repeatability of ± 0.5 μm, and a maximum velocity of 46.875 mm/s. The four dividing spindles have an indexing accuracy of 0.05°.
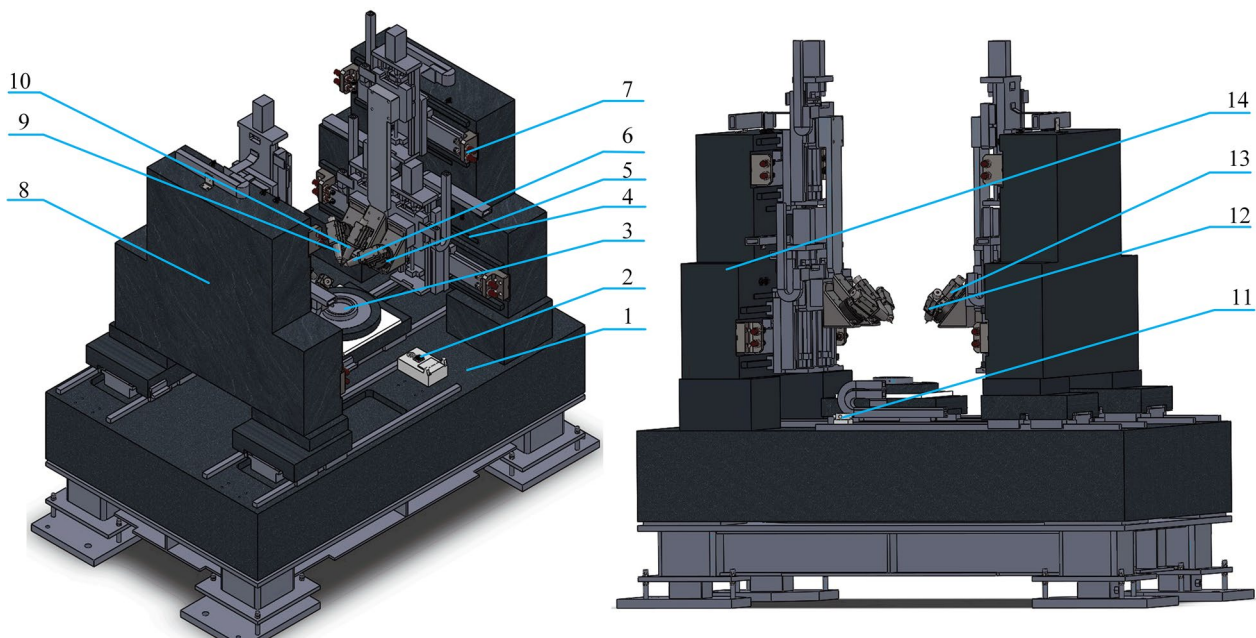

Figure 1 3D structural diagram of the 3D bioprinting platform with six printheads (1. Multi-axis motion platform, 2. Calibration module, 3. Printing stage, 4. Grating ruler, 5. Angle plate mechanism, 6. Temperature control printhead *N6*, 7. Limit switches, 8. Traveling gantry, 9. Temperature-control printhead *N5* , 10. Temperature-control printhead *N4*, 11. Receiver, 12. Temperature-control printhead *N2*, 13. Temperature-control printhead *N1*, 14. Fixed gantry)

The six printheads are distributed on the three moving axes installed on each gantry frame. The traveling gantry has three printheads, the fixed gantry has three printheads, which are in the same gantry, and the two printheads in the middle are fixedly connected to the printhead bracket. The four peripheral printheads are connected to the printhead bracket, are installed on the dividing head, can swing at a certain angle around the rotating mechanism, and have a manual dividing shaft. The printheads can move up and down (*Z*), and left and right (*Y*) as the gantry moves. Each printhead can move at any point in the *X-Y* plane.

In addition, each printhead can share three axial translation mechanisms and have independent degrees of freedom for movement. Therefore, the six printheads can simultaneously perform their own printing tasks at different positions. Each printhead assembly has its own printhead bracket, which has a fixed part connected to the *Z*-axis translation unit and a mounting part connected to the printhead assembly. The fixed and installed parts are at an inclination angle, thus the printhead assembly is inclined. The inclination of the printhead assembly indicates that it intersects the *Z*-axis at an angle, and the printing channels are obliquely set downward to avoid any movement interference between the storage barrels, enabling the multiple printheads to simultaneously work together. In addition, a guide rail slider structure was adopted for the traveling gantry. The printing vessel adsorbed on the workbench via vacuum adsorption was placed in the working area for the printing operation.

3.2 Feeding System

The feeding system is an important component of an extrusion 3D bioprinter. In this study, the feeding system was mainly composed of a temperature control printhead and pneumatic-temperature control system.

The printing temperatures of biomaterials and non-biomaterials mainly range from 0 to 220 °C. Based on this, the clamping temperature-controlled extrusion printhead was designed to maintain the printing materials warm, heated, and extruded.

The temperature-controlled printhead was designed as a temperature control clamping device that can position and fix the pneumatic material barrel to ensure the controllable position and posture of the material barrel on the platform, as well as control the temperature of the pneumatic material barrel, as shown in Figure 2. The temperature-controlled printhead includes a storage barrel, temperature control module, and printhead. The temperature control module includes an insulation barrel cover and the insulation barrel bottom. The storage barrel has a temperature control area wrapped by an insulation barrel cover and an insulation barrel bottom.
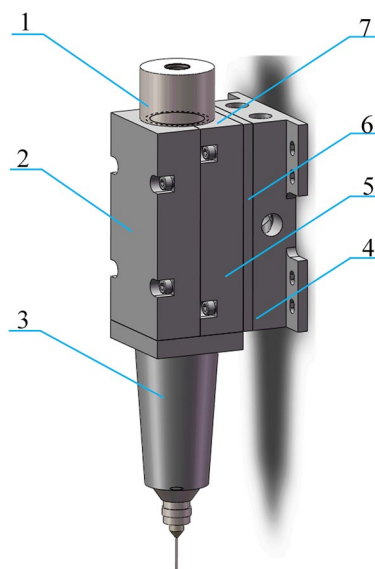

Figure 2 Design drawing of the temperature control printhead (1. Storage barrel, 2. Insulation barrel cover, 3. Insulation sleeve, 4. Water-cooling plate, 5. Insulation barrel bottom, 6. Insulation cotton, 7. Heating electrode)

The storage barrel between the temperature control area and printhead is the thermal insulation area, which is wrapped with a thermal insulation sleeve. The insulation barrel cover and the insulation barrel bottom are sealed and connected to form a medium cavity or medium pipeline, which is provided with a heating electrode. The heating electrode heats the medium in the medium cavity or medium pipeline, and the medium exchanges heat with the storage barrel to achieve the temperature control of the material in the storage barrel. The temperature control module includes a thermal insulation layer and a water-cooling plate. The thermal insulation layer is located between the bottom of the thermal insulation
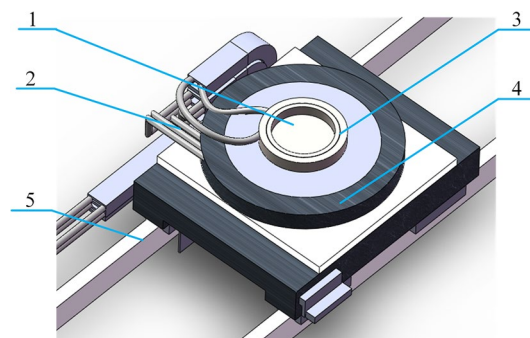

Figure 3 3D drawing of the printing stage (1. Printing vessel, 2. Temperature-controlled fluid medium pipeline, 3. Temperature control modules, 4. Print stage, 5. Guide rail)
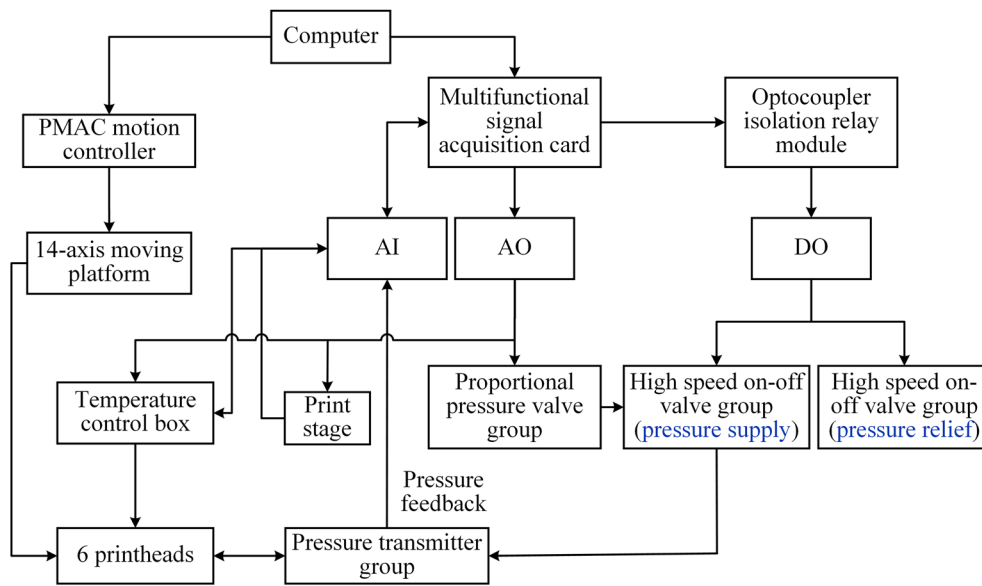
Figure 4 Block diagram of control system

bucket and the water-cooling plate. The water-cooling plate is connected to the printhead mounting piece, which is connected to the printhead bracket or rotating mechanism. The medium cavity or medium pipeline has a medium inlet and medium outlet, which are liquid heat-conducting media.

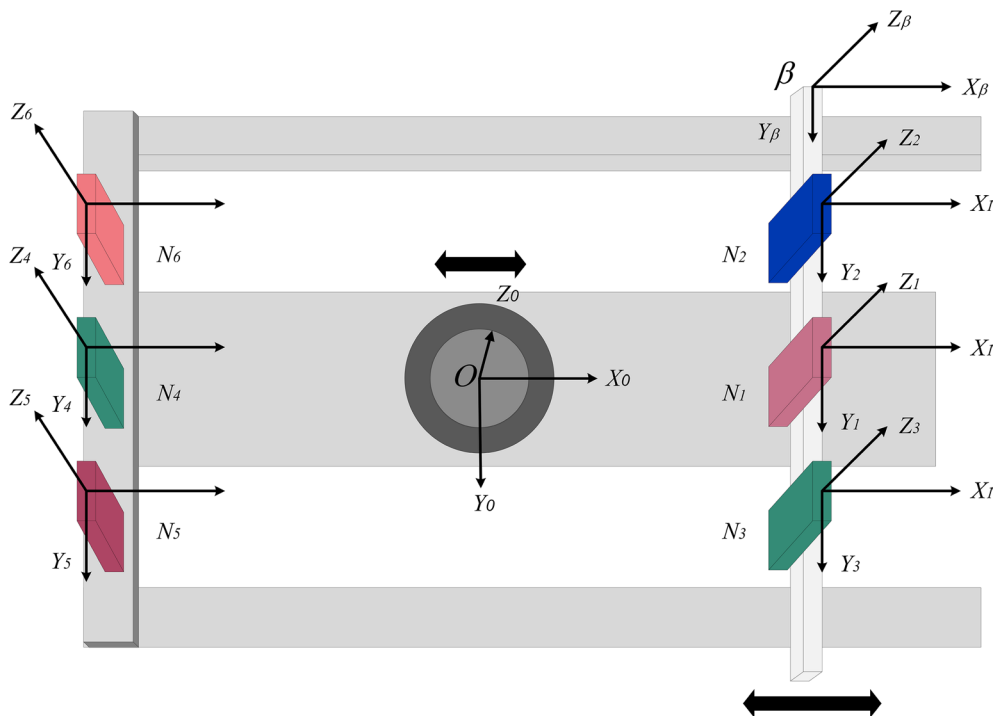The printing stage shown in Figure 3 is mainly composed of the printing utensils and temperature control modules. The heating pipe of the temperature-control

Figure 5 Schematic of the individual coordinate systems for each print module as well as the local coordinate system of the print stage and the associated global coordinate system of the multichannel bioprinter

Li *et al. Chinese Journal of Mechanical Engineering*   (2023) 36:140

Page 6 of 20

module is wrapped around the printing vessel. The printing vessel of the print stage is temperature controlled using a perimeter heat exchange. The medium is continuously circulated into the medium cavity after the temperature is accurately and easily controlled by the oil heater in the external medium container. The printing vessel is clamped by the bottom adsorption. The quantity of valve components is selected according to the size of the printing vessel to achieve a stable and complete adsorption of the working vessel. The outer peripheral temperature control, bottom vacuum adsorption, and clamping of the working vessel do not interfere with one another, which can reliably adsorb the working vessel, improve the accuracy of the molding structure, and consider the environmental temperature requirements in bioprinting. Hence, the quality of the molded living structure can be effectively guaranteed and the survival rate of living tissues can be improved. Furthermore, the temperature-controlled printing stage has a degree of freedom along the *X*-axis of the machine coordinate, and the temperature control module provides an ideal ambient temperature during the printing process. The temperature control of the printing stage and printheads was varied from 0 to 60 °C and from 0 to 240 °C, which is suitable for most biomaterials and non-biomaterials.

3.3 Control System

The control system of the multichannel 3D printing system consists of the following three subsystems: programmable multi-axis controller (PMAC) motion control, pneumatic extrusion control, and temperature control. Hence, in addition to the hardware design of the control system, the host computer program must be developed to efficiently and accurately control the three subsystems. Therefore, a block diagram was developed to visualize the printer control flow. Figure 4 presents a schematic of the generalized control flow of the 3D printer. Currently, the program design needs to be divided into the following three stages: The first stage is the development of the host computer program based on the PMAC motion control card to ensure that the input information of the man-machine interface and parameters can be operated at any time. The second stage would ensure that the communication channel between the upper and lower computers can be opened or closed at any time. The third stage would enable the special *G*-code to be interpreted and transmitted. In addition to the motion information being extracted for the PMAC, the pneumatic and temperature information can also be extracted for the PLC. Finally, the motion, pneumatic, and temperature controls of the multichannel 3D printing system are completely integrated by combining the PLC program and control operation program.

3.3.1 Coordinate Transformations

The primary challenge of dual-gantry-based multichannel collaborative printing technology is that the six printheads share the *X*-axis direction of motion, and there is a coupling relationship between the coordinate systems of the print stage, fixed gantry, and traveling gantry. The movement in the *X*-axis direction of the three printheads on the fixed gantry must be compensated by the *X*-axis movement of the print stage. The three printheads on the traveling gantry appear to be independent; however, their movement in the *X*-axis direction also depends on the *X*-axis movement of the traveling gantry. To accurately implement the printing task on the print stage, the *X*-axis movement of the traveling gantry must be linked to the *X*-axis movement of the print stage. Extrusion-based single-printhead 3D printing techniques (such as fused filament fabrication and direct ink write) typically rely on a point-to-point printing scheme, *G*-code, with toolpaths generated from the cross-sectional slices of solid models. Therefore, printing in parallel with multiple printheads requires switching between materials (*G*-code), while maintaining the accurate positioning of each module. To reliably coordinate the movement between different printheads and maintain accurate positioning, a kinematic transformation must be performed and applied to the generated print coordinates, as shown in Figure 5.

The executable *G*-code generated by a common slicing software provides a tool path in a local coordinate frame *O* on the printing platform. These coordinates cannot be directly used because the movement of the multichannel printer is determined by the motion controller and its respective coordinate system. To move between different printheads using *G*-code coordinates (denoted by N_i), a transformation matrix must be derived, which can represent the *G*-code associated with the printhead being used. First, the printing point *O* is considered as the origin, and the machine coordinate system *O* (X_0 Y_0 Z_0) is established. A relative coordinate system *β* (X_β Y_β Z_β) with respect to *O* on the traveling gantry is then established.

First, the *X* movement of the print stage and the traveling gantry are defined as X_0 and X_1, respectively. The movement of the coordinate system *β* relative to the coordinate system *O* is only the movement of the *X*-axis of the print stage; the translation matrix is as follows:

$$^O T_\beta = \begin{bmatrix} 1 & 0 & 0 & X_0 \\ 0 & 1 & 0 & 0 \\ 0 & 0 & 1 & 0 \\ 0 & 0 & 0 & 1 \end{bmatrix}. \tag{1}$$

The *X*-direction movement of the print stage is combined with the *Y*-direction and *Z*-direction movements of

the three printheads on the fixed gantry. The translation of the three printheads on the fixed gantry depends on the printhead being used, which is denoted as i and has values of 4, 5, and 6, and the offsets associated with the particular printheads Y_i and Z_i. Then, the transformation matrix $^O N_i$ of the three fixed gantry printheads based on the origin O is as follows:

$$^O N_i = {^O N_{ix}}{^O N_{iY}}{^O N_{iZ}} = \begin{bmatrix} 1 & 0 & 0 & X_0 \\ 0 & 1 & 0 & Y_i \\ 0 & 0 & 1 & Z_i \\ 0 & 0 & 0 & 1 \end{bmatrix}. \qquad (2)$$

The translation of the three printheads on the traveling gantry depends on the printhead being used, which is denoted as j and has the values of 1, 2, and 3, and the offset associated with the particular printhead Y_j and Z_j, which places the origin of the frame β at the point of the printhead. Similarly, the motion transformation matrix $^{\beta} N_j$ of the three printheads on the traveling gantry in the β coordinate system is as follows:

$$^{\beta} N_j = {^{\beta} N_{jx}}{^{\beta} N_{jY}}{^{\beta} N_{jZ}} = \begin{bmatrix} 1 & 0 & 0 & X_1 \\ 0 & 1 & 0 & Y_j \\ 0 & 0 & 1 & Z_j \\ 0 & 0 & 0 & 1 \end{bmatrix}. \qquad (3)$$

Any coordinate in the *G*-code can be described in terms of a frame O with a simple vector O_G from the origin O as follows:

$$O_G = \begin{bmatrix} X \\ Y \\ Z \\ 1 \end{bmatrix}, \qquad (4)$$

where *X*, *Y*, and *Z* are the coordinates of the *G*-code. Finally, through the translation matrix, any generated point in the *G*-code, *G*, can now be represented in the
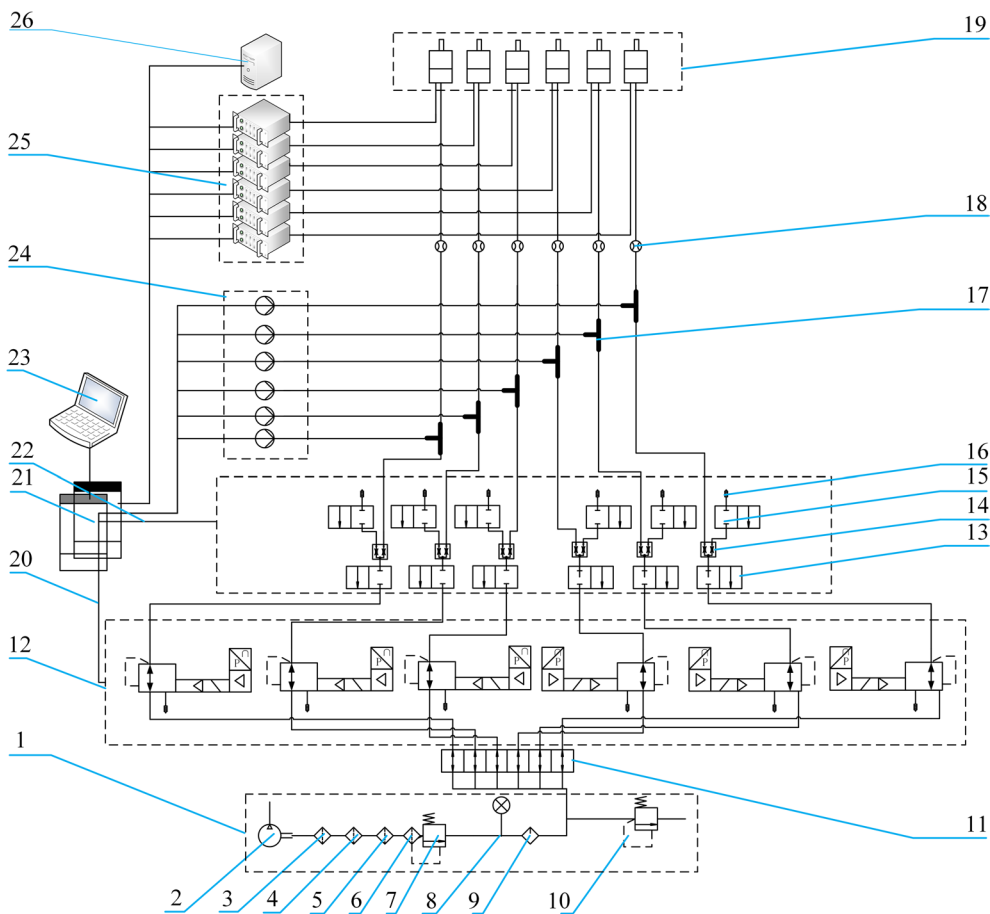

Figure 6 Schematic diagram of the pneumatic extrusion system (1. Air source processing module, 2. Air pump, 3. 40 μm filter, 4. 5 μm filter, 5. 1 μm filter, 6. 0.1 μm filter, 7. Safety (pressure reducing) valve ①, 8. Pressure gauge, 9. Dryer, 10. Pressure reducing valve ②, 11. Gas circuit board, 12. Proportional pressure valve group, 13. High speed on-off valve group ①, 14. Y-joint, 15. High speed on-off valve group ②, 16. Muffler, 17. *T*-joint, 18. Gas flowmeter, 19. Extrusion printhead, 20. Communications wiring, 21. Multifunctional signal acquisition card, 22. Communications wiring, 23. Computer, 24. Pressure transmitter, 25. High precision semiconductor thermostatic control box, 26. Oil heater)

coordinates of the motion controller for the respective printhead, j, on the traveling gantry and defined through the matrix equation represented as follows:

$$^{O}\boldsymbol{G}^{j} = {}^{\beta}\boldsymbol{N}_{j}{}^{O}\boldsymbol{T}_{\beta}\boldsymbol{O}_{G} = \begin{bmatrix} X + X_0 + X_1 \\ Y + Y_j \\ Z + Z_j \\ 1 \end{bmatrix}. \tag{5}$$

Furthermore, the respective printhead i on the fixed gantry is expressed as follows:

$$^{O}\boldsymbol{G}^{i} = {}^{O}\boldsymbol{N}_{i}\boldsymbol{O}_{G} = \begin{bmatrix} X + X_0 \\ Y + Y_i \\ Z + Z_i \\ 1 \end{bmatrix}. \tag{6}$$

3.3.2 Hardware Design of Motion Control System

The motion control system is based on the Delta Tau PMAC commercial controller. A PMAC is an open-mode multi-axis motion controller that can complete various types of functions with different types of motors, amplifiers, drives, etc. [39]. It can measure the relevant data in the surrounding motion state, and then achieve the communication task of the control data through the upper and lower computers to finally complete the control operation. The PMAC motion controller in the multichannel 3D printing system in this study was connected to 14 encoders, Hall sensors, a grating ruler, and 14 stepping motors. The dual X-direction movement composed of a traveling gantry and print stage was directly driven by a linear motor, and the Y- and Z-direction worktables were driven by servo motors linked to the ball screw. The displacement of each axis in the G-code was interpreted and converted into the number of pulses, which were distributed to the counterpart motor through the encoder controlled by the upper computer. The displacement and speed of each axis were fed back to the upper computer using a grating ruler and Hall sensor. To achieve an accurate control of the motor through the position feedback and speed feedback control methods, the real-time displacement and speed were compared with the set displacement and speed in real-time. Finally, multi-axis high-precision motion independent control of the 3D printing system was conducted.

3.3.3 Pressure and Temperature Control System Design

When the multichannel 3D printing system operates, the motion subsystem, printhead pneumatic extrusion control subsystem, and temperature control subsystem cooperate with one another. To achieve synchronous printing or concurrent printing with the six printheads, the following functional requirements should be met: the air pressure control belongs to the pneumatic extrusion control subsystem and the temperature control belongs to the temperature control subsystem, the
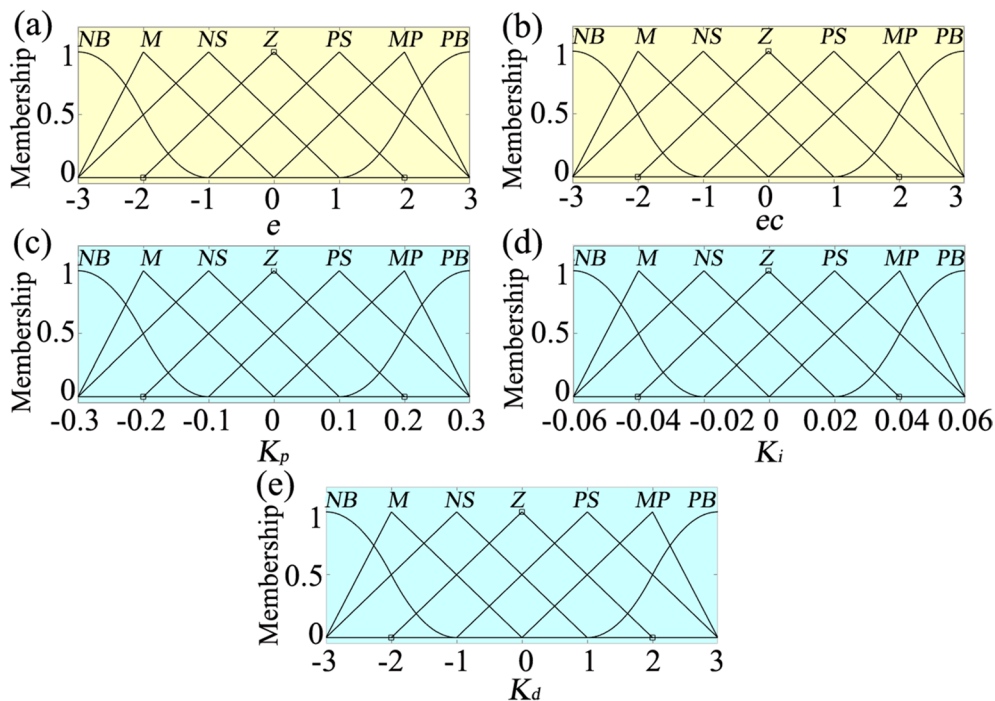

Figure 7 Fuzzy membership function

Li *et al. Chinese Journal of Mechanical Engineering*   (2023) 36:140

Page 9 of 20

air pressure and temperature values required for the operation of the six printheads can be written through the program interface, the air pressure value will be transmitted to the corresponding six air pressure proportional pressure valves in real-time, and the temperature value will be transmitted to the corresponding six high-precision temperature controllers and oil temperature machine. In the printing process, all of the temperatures and pressures of the six printheads or the print stage are controlled independently. The function of the pressure supply and pressure relief, as well as the temperature setting need to rapidly respond to achieve

the real-time start and stop of the extrusion printing process. In addition, the air pressure and temperature in each extrusion printhead were controlled using real-time monitoring or closed-loop feedback.

As shown in Figure 6, the pressure and temperature control systems consider the upper computer and two multifunctional signal acquisition cards as the core. According to the functional requirements, each module circuit is designed and equipped with a processing program that achieves an accurate control of the air pressure and temperature.

Table 1 Fuzzy rules of K_p

K_p		ec						
		NB	NM	NS	ZO	PS	PM	PB
e	NB	NB	NB	NM	NM	NS	NS	ZO
	NM	NB	NM	NM	NS	NS	ZO	PS
	NS	NM	NM	NS	NS	ZO	PS	PS
	ZO	NM	NS	NS	ZO	PS	PS	PM
	PS	NS	NS	ZO	PS	PS	PM	PM
	PM	NS	ZO	PS	PS	PM	PM	PB
	PB	ZO	PS	PS	PM	PM	PM	PB

Table 2 Fuzzy rules of K_i

Ki		ec						
		NB	NM	NS	ZO	PS	PM	PB
e	NB	NB	NB	NM	NM	NS	ZO	ZO
	NM	NB	NB	NM	NS	NS	ZO	ZO
	NS	NB	NM	NS	NS	ZO	PS	PS
	ZO	NM	NM	NS	ZO	PS	PM	PM
	PS	NM	NS	ZO	PS	PS	PM	PB
	PM	ZO	ZO	PS	PS	PM	PB	PB
	PB	ZO	ZO	PS	PM	PM	PB	PB

Table 3 Fuzzy rules of K_d

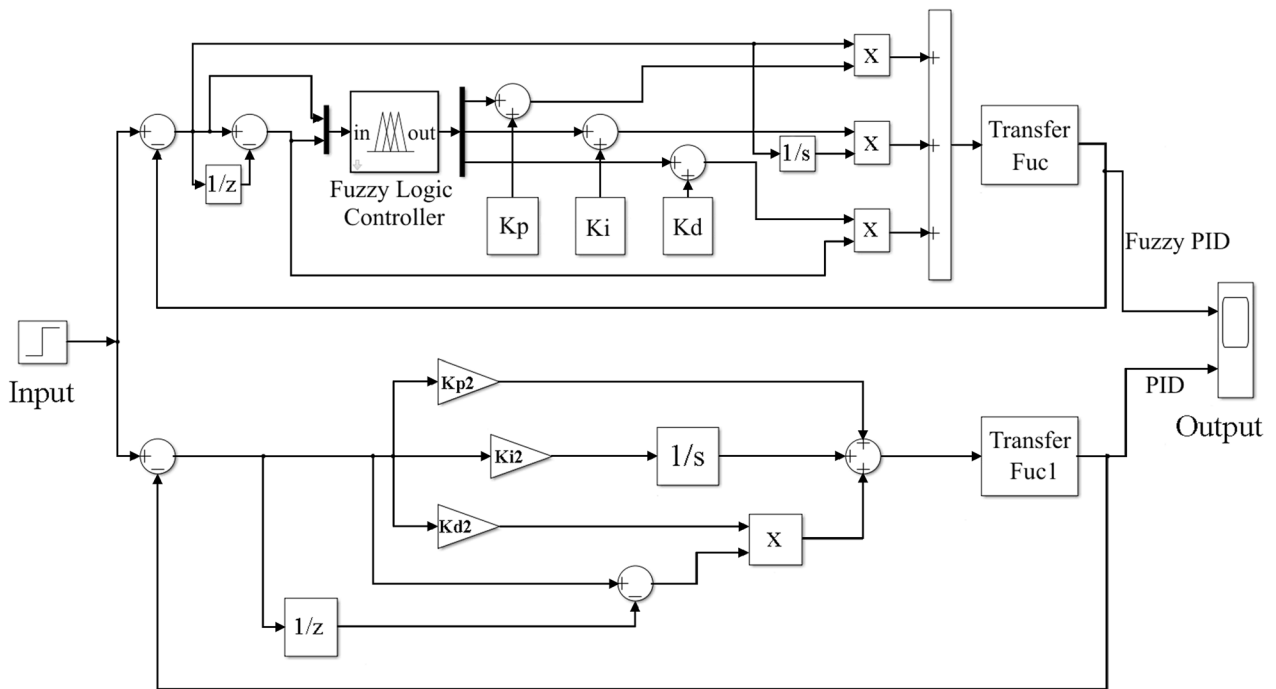| K_d		ec						
		NB	NM	NS	ZO	PS	PM	PB
e	NB	PS	NS	NB	NB	NB	NM	PS
	NM	PS	NS	NB	NM	NM	NS	ZO
	NS	ZO	NS	NM	NM	NS	NS	ZO
	ZO	ZO	NS	NS	NS	NS	NS	ZO
	PS	ZO	ZO	ZO	ZO	ZO	ZO	ZO
	PM	PB	NS	PS	PS	PS	PS	PB
	PB	PB	PM	PM	PM	PS	PS	PB

Figure 8 Simulink simulation model of fuzzy PID

The control of the temperature-control printhead is mainly composed of a high-precision semiconductor constant-temperature control box and an oil temperature machine. The actual temperatures of the temperature control printheads were collected by a temperature control box in real-time and compared with the input temperature to conduct feedback control. Finally, the

temperatures of the stage and each printhead were independently controlled.

The pneumatic extrusion system is the core control system of an extrusion-based 3D bioprinter. The air pressure control accuracy is an important factor affecting the stability of the extrusion speed in the printing process. In particular, for printing materials that can be
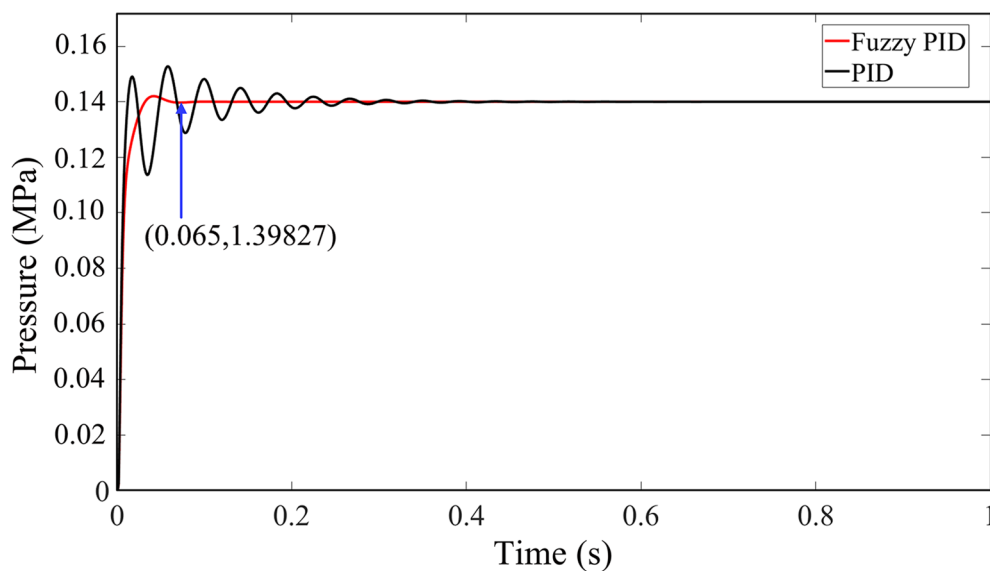

Figure 9 Contrast simulation curve of the step response

extruded under a low pressure, the air pressure stability has a greater impact on the stability of the extrusion speed. As shown in Figure 6, the pneumatic control system includes an air source processing module, air pressure control module, pressure supply and relief module, extrusion printhead, and feedback control module. In addition, strict sterilization and filtration measures, such as a step-by-step filtration system using four filters, were adopted to provide a clean and sterile air pressure. Then, 6-way stable pressures were obtained from the proportional pressure valve group consisting of six proportional-pressure regulators, which were linked to the air pump. Under the mutual cooperation of the two fast-switching valve groups consisting of six fast-switching valves with switching frequencies of up to 500 Hz, the functions of the real-time pressure supply and pressure relief are accomplished in the printing process, and the printing materials are extruded evenly and controllably. The filtered gas achieves the following three synchronous controls through the program: 1) gas pressure control of different printheads to achieve the pressure regulation function, 2) on-off of gas control to achieve the pressure supply function, and 3) discharge of the gas control to achieve the pressure relief function, accomplishing the real-time demand of the six printheads with any various materials under different pressures, as well as to ensure the continuous and controllable extrusion during the printing process. The pressure-relief time is controllable, which ensures that the gas will not remain in the pipeline.

Considering the aforementioned, the multichannel 3D bioprinter often needs to simultaneously supply gas to six printheads in the printing process, and the work of the exhaust system will also interfere with the pressure in the pipeline. To achieve a fast and accurate control of the 6-channel air pressure through the proportional pressure valve group, a fuzzy PID controller was applied to the pneumatic extrusion system. The controller combines the fuzzy control principle with the conventional PID control algorithm to achieve the online adjustment of the PID parameters and adjusts the cross-sectional area of the air flow by controlling the 6-way proportional pressure valves to realize the constant pressure control of the gas in the six printheads of the extrusion system.

According to the different states of the system operation, the correlations of K_p, K_i, and K_d are considered in the fuzzy PID control. The fuzzy rules are designed to adjust these three parameters online according to engineering experiences. The input variables were selected as the error e and deviation change rate ec, and the output variables were K_p, K_i, and K_d. The output state can be deduced based on these rules and the current input state. All variable values obtain {*NB*, *NM*, *NS*, 0, *PS*, *PM*, *PB*} seven fuzzy values, which represent the following: Negative large, negative medium, negative small, zero, positive
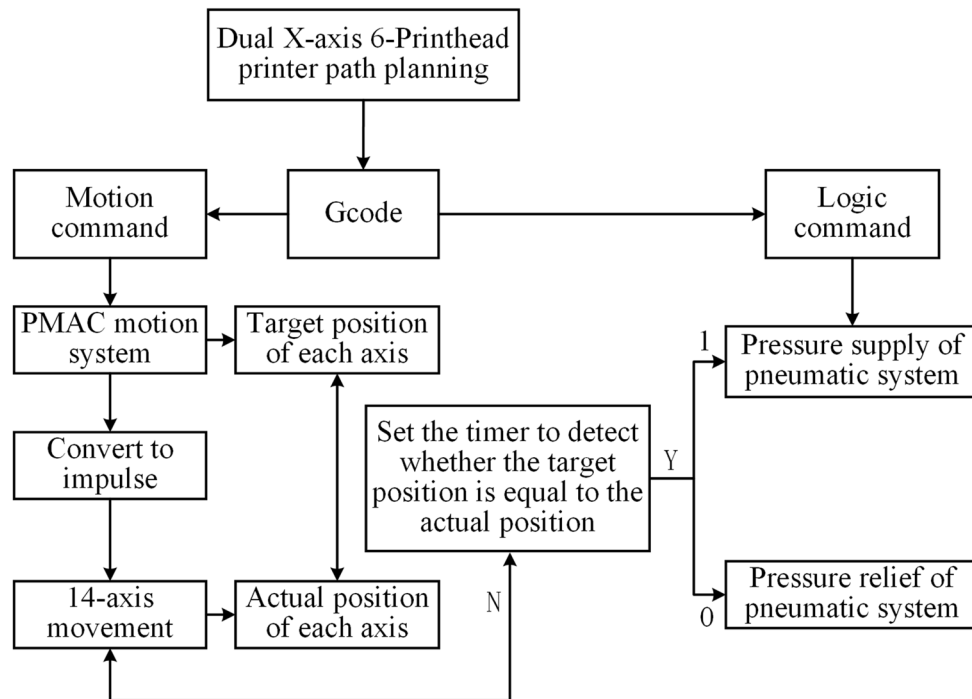

Figure 10 General algorithm or work-flow of multichannel 3D bioprinter, which was coded in C++ to develop the printer software

Figure 11 Front-end user interface (UI) for the parameter setting and data display

small, positive medium, and positive large, respectively. Triangular and normal membership functions are used for these variables; the theoretical domain of the input quantities e and ec are determined as $\{-3, 3\}$, and its fuzzy domain is determined as $\{-3, -2, -1, 0, 1, 2, 3\}$. The resulting membership functions for the errors in the fuzzy input quantities and the rate of change of the errors were determined as shown in Figure 7. The output quantity system control parameter correction values K_p, K_i, and K_d are determined for the theoretical domains of $\{-0.3, 0.3\}$, $\{-0.06, 0.06\}$, and $\{-3, 3\}$, respectively, where the fuzzy theoretical domains are $\{-0.3, -0.2, -0.1, 0, 0.1, 0.2, 0.3\}$, $\{-0.06, -0.04, -0.02, 0, 0.02, 0.04, 0.06\}$, and $\{-3, -2, -1, 0, 1, 2, 3\}$, respectively. The negative large and positive large membership functions will be the same, which are set to zmf-shaped and smf-shaped functions; the others are set to triangle functions. K_i and K_p are determined with the K_d fuzzy membership function of ri, as shown in Figure 7.

In this study, the Mamdani algorithm was used for fuzzy inference, and the fuzzy control rule table was established [40]. As shown in Tables 1, 2, 3, the 7-level symmetric fuzzy space segmentation and fuzzy sets ranging from small to large were applied at the input and output domains.

The conventional PID control algorithm and fuzzy PID algorithm were built in MATLAB Simulink according to the control requirements and control system design of the 3D printing gas supply system. Because the six gas circuits had the same structure, one of them was

selected for the simulation experiment. The conventional and fuzzy PID control simulation models are shown in Figure 8.

After the simulation model was built, combined with the actual situation of the project, the expected value was set to 0.14 MPa, and the initial parameters of the PID were tuned by the critical ratio method. Under the condition of the step input, the simulation results of the two algorithms were analyzed and compared. The simulation results of the fuzzy and conventional PID controls are shown in Figure 9.

The air pressure in the pneumatic control system based on the proportional pressure valve group was adjusted according to the adaptive fuzzy PID controller and the conventional PID controller designed in this study. The step and disturbance responses of the system are shown in Figure 9, which demonstrates that under the same input conditions, the gas pressure starts from the initial value 0 and can reach the set value and become steady after a certain period of time. Both the conventional and fuzzy PID control methods can achieve gas pressure control. However, with the fuzzy PID control method, the gas pressure rise curve is relatively stable, the overshoot is significantly reduced, and the adjustment time is shortened.

3.3.4 Software System Design

In the process of developing the control system, the functions of data acquisition and real-time display for the motion, pneumatic, and temperature subsystems were
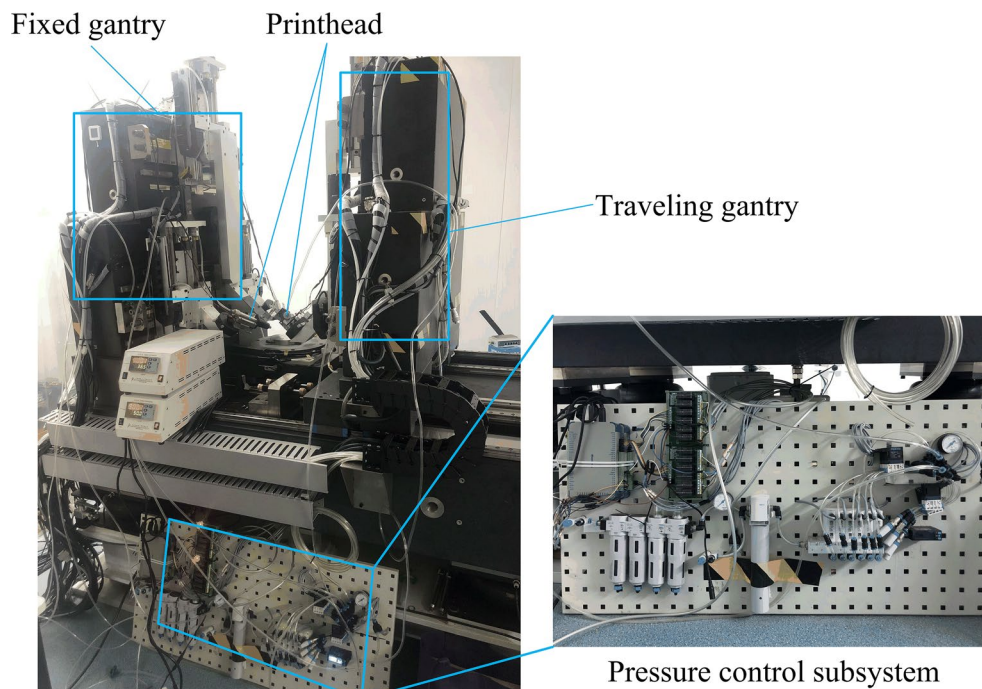
Figure 12 Multichannel 3D bioprinting platform (image on the left presents the motion platform and printhead; image on the right presents the pneumatic and temperature control system)

added to the motion control system based on PMAC. Therefore, a flowchart was developed to visualize the work flow of the printer. Figure 10 presents a schematic of the generalized workflow of the multichannel printer. That is, four functional procedures including the real-time display of the 14-axis position and speed parameters; the real-time display of the processing code; the pressure setting and its real-time display; the temperature setting and display are developed.

These functional programs are mainly run on windows10 and have been repeatedly debugged and modified in Visual Studio 2017 to ensure correctness and feasibility. The program in the platform was developed and debugged by the language editor. This communication function can be used as a communication bridge between the upper and lower computers. To compile the C++ mode control program, the dynamic linking library PCOMM32 functions as PCOMM32. DLL is implemented using PMAC to control the movement of the platform and the function of the real-time feedback. A user-friendly interface printer software was developed to assist users, as shown in Figure 11.

The data acquisition program of the control system based on PMAC was achieved by improving the program through the PID algorithm. The PID algorithm needs to have the following three independent parameters for calculation: motion, pressure, and temperature. These

parameters can be extracted from the PMAC function repository. The independent parameters of the PID algorithm are set as K, T, and B, respectively, the output value in the algorithm is $\eta(t)$, and the input value is $Q(t)$. The proportional and calculus relationships in this algorithm can be obtained using the following formula:

$$\eta(t) = K\left[Q(t) + \frac{1}{T}\int Q(t) + B\frac{t}{d}\right], \tag{7}$$

where d represents the time error and t represents the calculus time constant. This formula achieves the data acquisition of the speed, air pressure, and temperature in the computer control system in the following form:

$$\eta(t) = K\left[Q(t) + \frac{1}{T}\sum_{i=1}^{K} Q(t)\right], \tag{8}$$

where K represents the data acquisition sequence of the computer and T represents the operation cycle of the control system.

The main program interface of the operation interface for the control system based on the PMAC designed in this study was determined by printing experiments. As shown in Figure 11, the input and output values of the 14-axis motion corresponding to the 14-motors, the air pressure parameters, and the temperature parameters of the six temperature-control printheads and *G*-code were
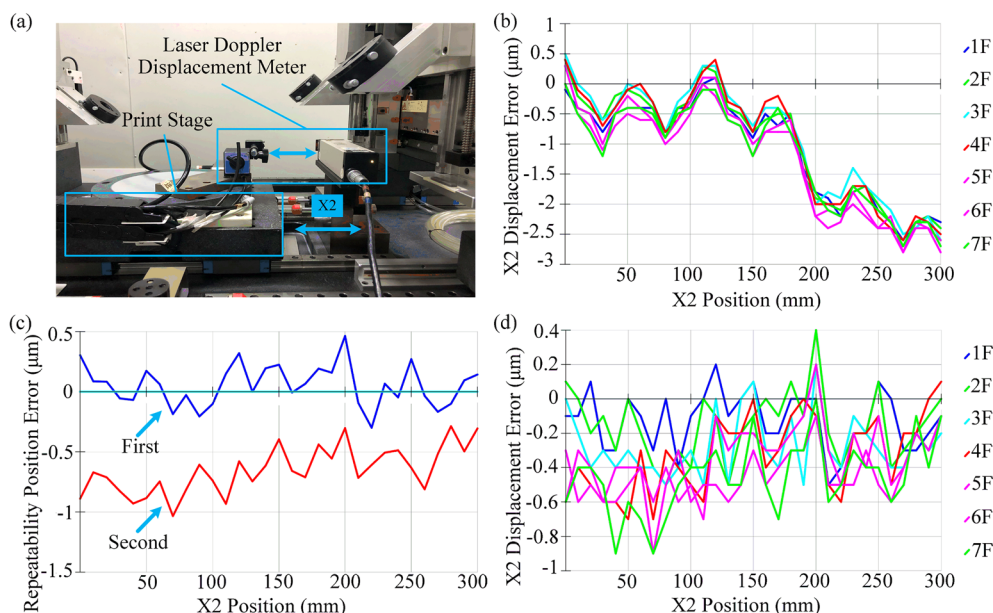
Figure 13 Motion accuracy detection

set or displayed, respectively. The SN code of the two multifunctional data acquisition cards can be automatically identified by the upper computer to ensure the corresponding function of each signal acquisition card.

4 Experimental Process and Analysis

4.1 Multichannel 3D Bioprinting Platform Set Up

Figure 12 presents images of the assembled printer. The 3D printing process of bio-extrusion can be decomposed into the height superposition of multilayer printing. During the printing process of each layer, the printhead moves at a certain speed in the *XY* plane according to the planned path. Because the response speed and control accuracy of the air pressure control are lower than that of the printhead movement control, when the print head is designed to move in the *XY* plane, the set value of the air pressure remains unchanged. The moving speed of the printhead is controlled through a pressure closed loop, enabling the moving speed of the printhead to be adjusted in real-time with small changes in air pressure to ensure a high consistency of the extruded fiber line diameter.

According to the planned path, the movement of the printhead in the *XY* plane is divided into the following three cases: *X-, Y-,* and *XY*-axis cooperative movements. Path planning was completed using the slicing software of the upper computer. The single-chip microcomputer processor calculates the moving speed of the printhead in the *XY* plane in real-time

according to the feedback signal of the pressure sensor and decouples the displacement and speed of the printhead in the *X* and *Y* directions according to the print path and air pressure value. Then, the single-chip microcomputer processor sends control instructions to the *X-* and *Y*-axis servo motor drivers and moves through the linear module to achieve the cooperative movement of the printhead in the *XY* plane. Six model files were imported into the slicing software of the upper computer, the filling parameters were set, and a 6-axis linear path slicing path library was generated. The serial instruction of the 6-axis robot was transformed into a parallel instruction. The command mode was converted to [G $X1$ $X2$ $Y1$ $Y2$ $Y3$ $Y4$ $Y5$ $Y6$ $Z1$ $Z2$ $Z3$ $Z4$ $Z5$ $Z6$ $T1$ $T2$ $T3$ $T4$ $T5$ $T6$], yielding a total of 21 parameters. The left and right printheads were controlled by $X1$ and $X2$, respectively, and six parameters of air pressure from $T1$ to $T6$ were added. $T1$ to $T6$ are controlled by the binary numbers 0 and 1, where 0 represents closed and 1 represents open, to control the pressure supply and relief of the six printheads.

4.2 Motion Accuracy Detection and Error Compensation

Considering that the motion structure of each axis of the printer is the same, the displacement error (positioning accuracy) of the *X*-axis motion (*X*2) of the print stage was detected and identified by a laser doppler displacement meter (LDDM) MCV-500 (OPTODYNE, Compton, CA, USA) in this study. The layout of the measurement
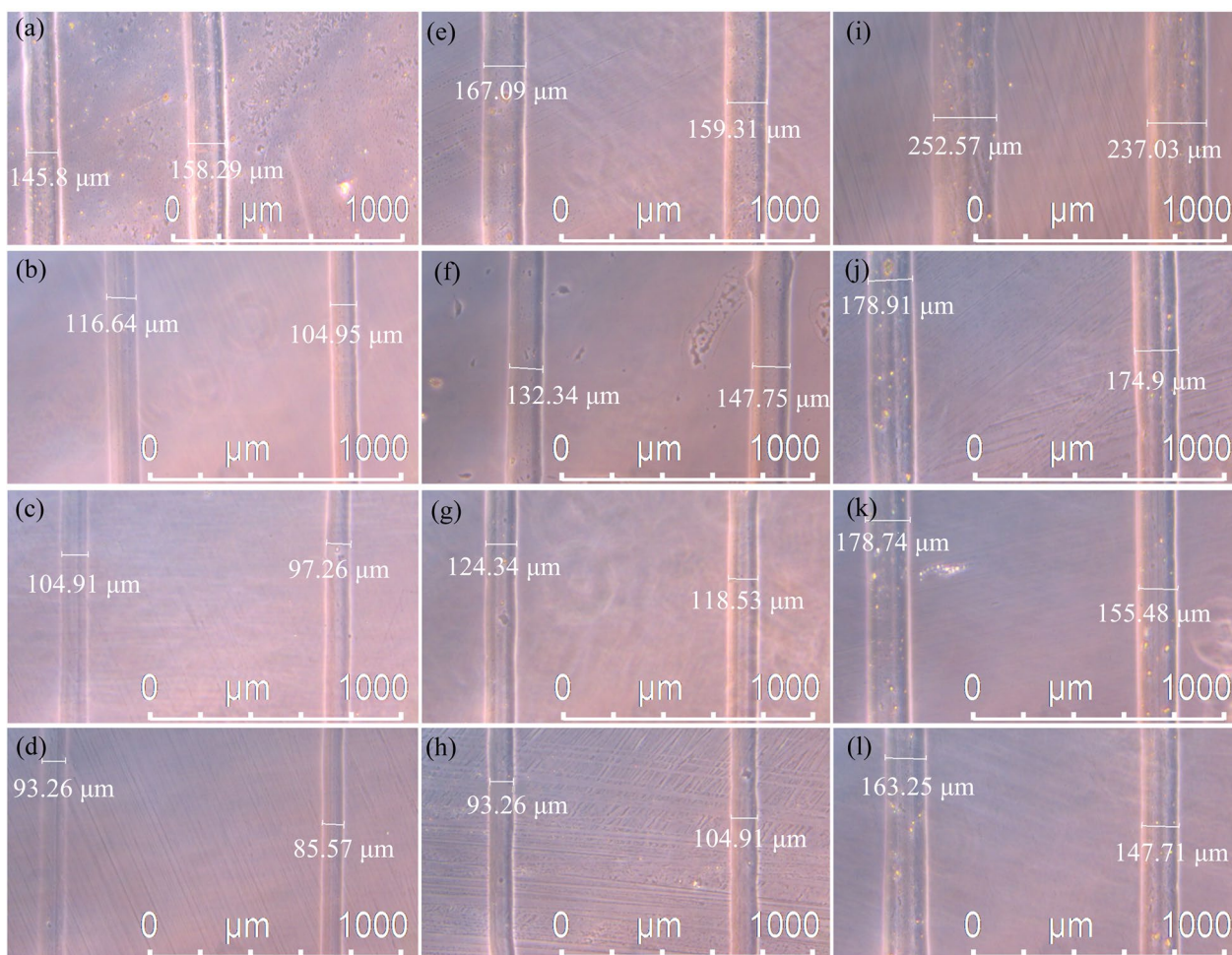
Figure 14 Images of the printing filaments with different printheads at various moving speeds

system is such that the linear mirror is installed on the print stage and the laser head is installed on the printer platform because the common optical path system is adopted in MCV-500, as shown in Figure 13(a). The displacement error in which the beam from the laser head is reflected back to the laser head directly by the linear mirror is obtained according to the laser doppler frequency difference effect. After detection, we found that there was a certain error in $X2$. The displacement error curve based on the detection results is shown in Figure 13(b), which demonstrates that the error range is between -3 to $+0.5$ μm.

After determining the displacement error of $X2$, the compensation value is imported into the PMAC in the form of a compensation table enable according to the concept of error compensation [41]. According to the remeasurement results, the compensated error curve and repeated positioning accuracy curve are shown in Figure 13(d) and (c), respectively. Through a comparative analysis, the motion accuracy of $X2$ was observed

to significantly improve after conducting an error compensation. The compensated displacement error range is mainly distributed between -0.6 and 0 μm, which is an increase of nearly 580%, and the repeated positioning accuracy is controlled within 1 μm. In addition, the accuracy measurement and error compensation are conducted for the other 13 axes in turn through these measurement and compensation methods, enabling the motion accuracy of the printer to be controlled at the submicron level.

4.3 Print Accuracy Test

The printing speed was also one of the most influential factors in the extrusion forming process. If the speed is too high, the forming filament will be too thin and easily cause breakpoints. In contrast, a speed that is too low will cause excessive hydrogel to diffuse outward, causing it to be deposited at an inaccurate position. Therefore, the printing accuracy of the printer was verified by changing the printing speed.
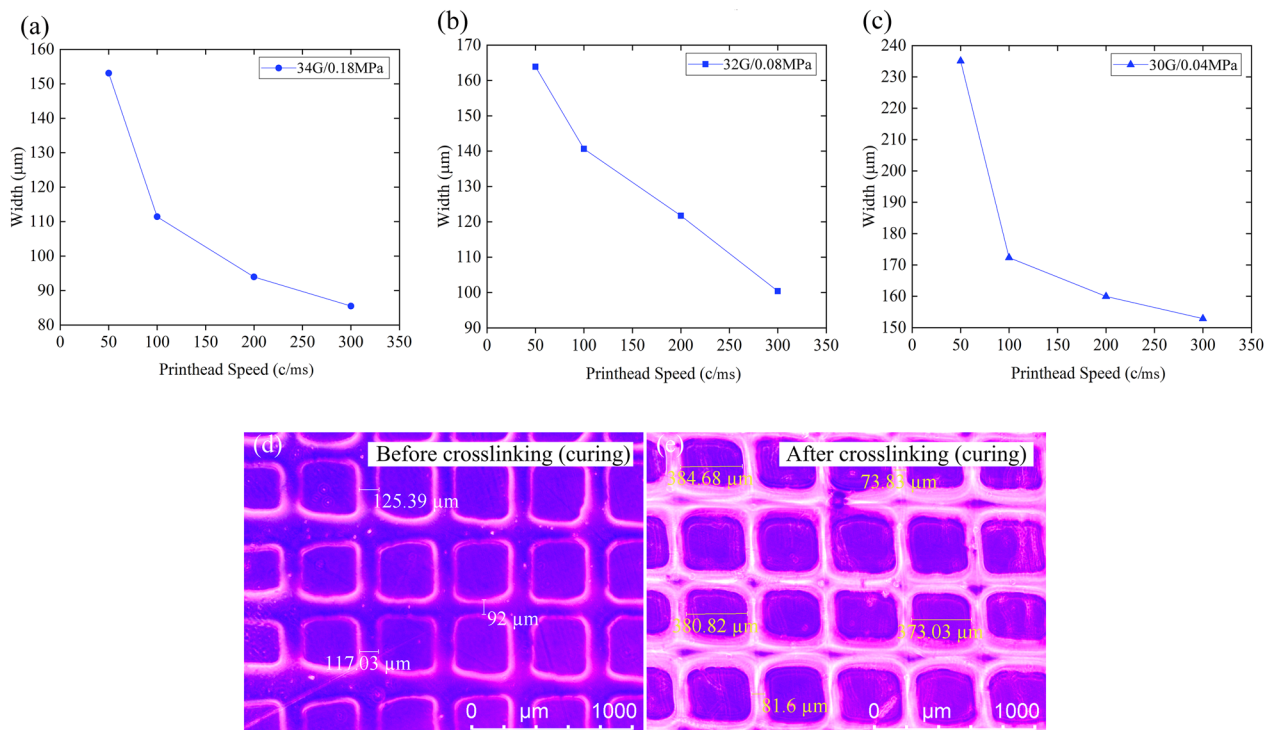
Figure 15 High precision printing experiment of a biomaterial: **a**–**c** Change curve of the extruded filament widths with the printing speed and hydrogel scaffold, **d**–**e** Hydrogel scaffold
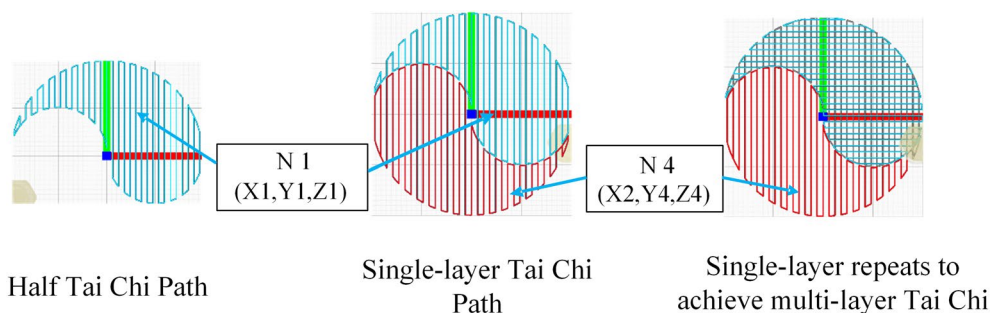

Figure 16 Dual printhead printing path planning

This experiment was designed to verify the bioprinting accuracy and effectiveness of the printer construction using a hydrogel with a composition of 3% w/v alginate and 1% w/v gelatin (marked as 3A1G). It was dissolved in deionized water (conductivity of 0.07 μS). Sodium alginate (Sigma-Aldrich, Saint Louis, MO, USA), gelatin (Sigma-Aldrich, Saint Louis, MO, USA), and calcium chloride were used as a cross linker (Sigma-Aldrich, Saint Louis, MO, USA). The stainless-steel dispensing machine needles were selected as printheads, whose specifications were 34G, 32G, and 30G, and the respective inner/outer diameters were 0.04/0.23, 0.08/0.23, and 0.15/0.29 mm.

Through the pre-extrusion experiment at a room temperature of 25 °C, the hydrogel was tested to be uniformly extruded by 34G, 32G, and 30G at pressures of 0.18, 0.08, and 0.04 MPa, respectively. In addition, because the maximum speed of the printer was 300 c/ms (46.875 mm/s), the design experiment was as follows: Under the corresponding uniform extrusion pressure of the different printheads, the wire diameter was tested, which was extruded under the printheads' *Y*-axis displacement of 10 mm and movement speeds of 50 c/ms (7.8125 mm/s), 100 c/ms (15.625 mm/s), 200 c/ms (31.25 mm/s), and 300 c/ms (46.875 mm/s), respectively. Repeated experimental
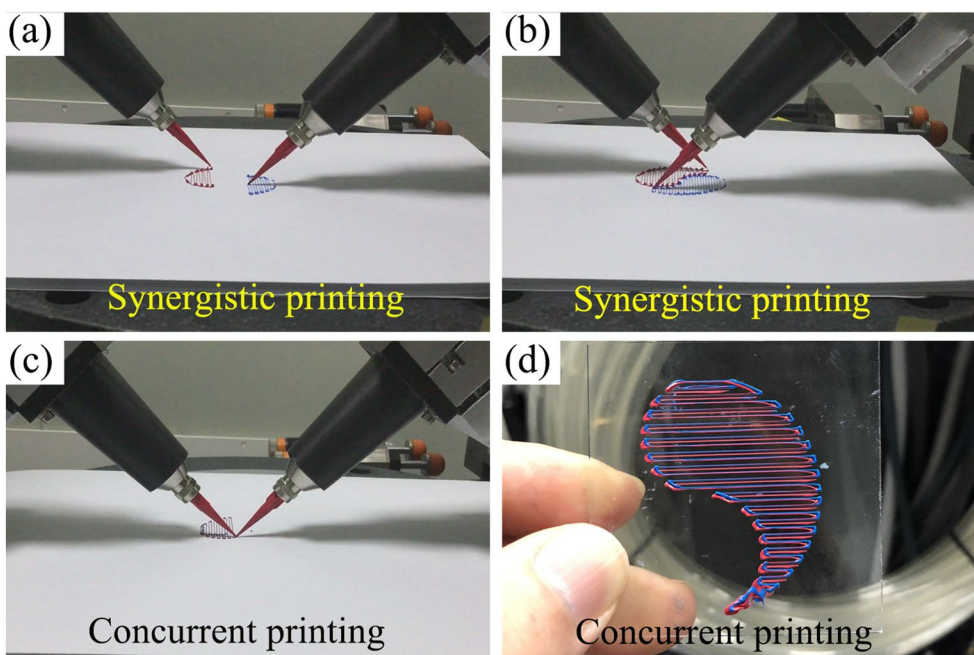
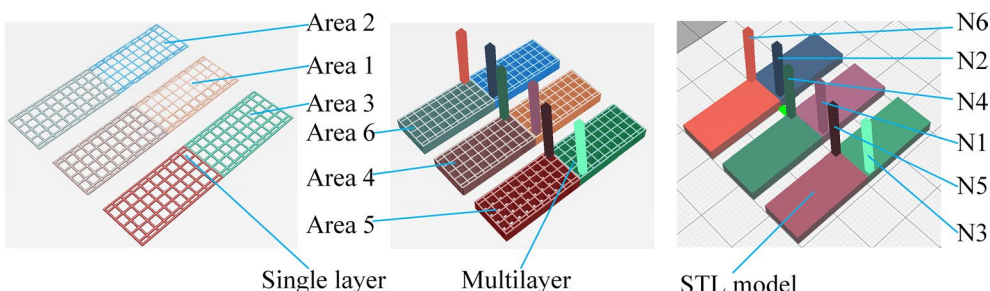**Figure 17** Dual printhead experiment

Figure 18 Multichannel synergistic printing path planning

tests were performed to express the bioprinting accuracy, and the final results are shown in Figure 14.

Figures 14 and 15(a)–(c) demonstrate that the filament width decreases with an increase in the printhead speed. When the speed increased from 50 c/ms (7.8125 mm/s) to 300 c/ms (46.875 mm/s), the filament width decreased from 152.0 to 89.4 μm by printhead 34G (Figure 14(a)–(d)), and from 163.2 to 99.1 μm by printhead 32G (Figure 14(e)–(h)), as well as from 244.8 to 155.48 μm by printhead 30G (Figure 14(i)–(l)). However, the decreasing trend of the filament width of the printheads with the various specifications are slightly different, which is related to the pressure, temperature, and structural properties of the printhead. In addition, Figure 14 demonstrates that all the hydrogel filaments

were steady, uniform, and accurate, which revealed that the printer combined with the three different specifications of the printheads can ensure a uniform and stable filament formation by adjusting the air pressure within the allowable range of the printer speed, which is confirmed in Figure 15(d) and (e), a 3A1G hydrogel scaffold printed by 32G with a velocity and pressure of 290 c/ms (43.75 mm/s) and 0.04 MPa, respectively. The hardware structure of the printer was also demonstrated to be stable with a high positioning accuracy and further illustrates the good coordination and control performance of its hardware system and feeding system, which ensures a high-precision and stable extrusion performance for accurately building transplantable organs or tissues.
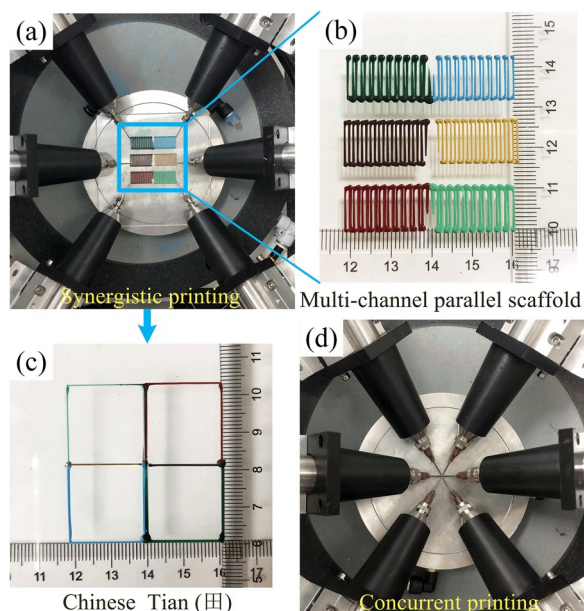
Li *et al. Chinese Journal of Mechanical Engineering*   (2023) 36:140

Page 18 of 20

Figure 19 3D printing experiment with 6 printheads

4.4 Synergistic Printing and Concurrent Printing Experiment by Dual-Printhead

To test the synchronous and concurrent printing functions of the printer, silicone rubber was selected as the printing material. For dual-printhead printing, the printing model Tai Chi was selected, and its trajectory planning model is shown in Figure 16. The internal filling of the printing model was filled with a grid composed of 0° and 90° cross straight lines. Click-start printing was used to conduct the printing experiment. The printing results are shown in Figure 17.

4.5 Multichannel Concurrent and Synergistic Printing

For synergistic printing with 6 printheads, acrylic paint was selected as the printing material for synergistic printing with six printheads. A structure with a length × width × height of 30 mm× 40 mm× 2 mm was selected for the printing experiment. The slicing results are shown in Figure 18, which demonstrates that the six printheads work synchronously. In the printing process, the upper computer interprets and executes the *G*-code to control the 14-axis motion platform to work together with the pneumatic extrusion system. To achieve the cooperative movement of multiple printheads, the STL model was automatically divided into six areas. Each of the areas corresponds to a printhead, and will simultaneously call a slicing program once to generate the *G*-code, which includes the displacement of each axis and the real-time control code of the real-time start and stop of the

multichannel pneumatic. The printing results are shown in Figure 19(a) and (b).

For collaborative printing with an unfixed number of channels (3, 4, or 5), a Chinese character Tian (田) was selected for the printing experiment, as shown in Figure 19(c). In addition, if *X*1 is always zero, and all the *Y*-axis displacements are the same, that is, concurrent printing. Based on this perspective, the multichannel 3D printer has a high flexibility in the use of printheads, which can be arbitrarily switched according to the needs from 1 to 6.

5 Conclusions

(1) Combined with the development of 3D printers and the demand for precision manufacturing of organs in vitro, a synergistic printing method and concurrent printing method were proposed. Based on these printing strategies, a multichannel 3D bioprinting platform with 18 motion degrees of freedom was developed in this study, which has a motion accuracy of the submicron level to meet the requirements of high-precision printing.

(2) Through the development of a control system based on PMAC and the fuzzy PID control of the multichannel pneumatic, the coordinated control of the multichannel pneumatic and 18-axis motion platform was achieved, and the synergistic and concurrent printing methods of the multiple printheads was achieved.

(3) Through the actual measurement of LDDM, the displacement error range was mainly distributed between −0.6 and 0 μm after conducting an error compensation. The motion accuracy of the printer was verified to reach a submicron level.

(4) The high-precision printing of non-biomaterials and biomaterials was experimentally achieved. The filament width printed by printheads with three different sizes had a small diameter and high straightness, which demonstrates the excellent printing performance of the 3D printer and verifies its reliability and control system.

(5) The cooperative printing between six printheads was experimentally achieved, and the synchronous and concurrent printing effects of the multichannel 3D bioprinter were verified.

Authors' information
Jintao Li, is currently a PhD candidate at *State Key Laboratory of Fluid Power Transmission and Control, School of Mechanical Engineering, Zhejiang University, China*. He received his master's degree from *Northeastern University, China*, in 2018. His research interests include path planning and coordinated control of 3D bioprinting with multichannel.
Bin Zhang, received his PhD degree in Engineering from *Zhejiang University China*, in 2009. Currently, he is a researcher at *School of Mechanical Engineering, Zhejiang University, China*. His research interests include intelligent digital hydraulics and bio-manufacturing based on fluid extrusion.
Yichen Luo, received his B.S. degree from *Southeast University, China*, in 2015. He is currently a PhD candidate at *State Key Laboratory of Fluid Power Transmission and Control, School of Mechanical Engineering, Zhejiang University, China*.
Huayong Yang, received his PhD degree from *University of Bath, United Kingdom*, in 1988. He is the dean of *School of Mechanical Engineering, Zhejiang University, China*. He was elected as an academician of *Chinese Academy of Engineering* in 2013. His research interests include electro-hydraulic control components and systems, energy saving in hydrodynamic and electromechanical systems, and bio-manufacturing.

Declarations

Competing Interests
The authors declare no competing financial interests.

References

[1] D J Roach, C M Hamel, C K Dunn, et al. The m4 3D printer: A multi-material multi-method additive manufacturing platform for future 3D printed structures. *Additive Manufacturing*, 2019, 29: 100819.

[2] C W Hull. Apparatus for production of three-dimensional objects by stereolithography: US, 4575330 A. 1986–03–11[2022–05–13]. https://www.google.com/patents/US4575330A.

[3] C B Ahn, K H Son, J W Lee. 3D printing technology and its applications for tissue/organ regeneration. *Journal of the Korean Society for Transplantation*, 2015, 29(4): 187–193.

[4] D X Cheng, C Wei, Y H Huang, et al. Additive manufacturing of lithium aluminosilicate glass-ceramic/metal 3D electronic components via multiple material laser powder bed fusion. *Additive Manufacturing*, 2022, 49: 102481.

[5] J Q Zhang, Y G Liu, G Sha, et al. Designing against phase and property heterogeneities in additively manufactured titanium alloys. *Nature Communications*, 2022, 13: 4660.

[6] N Li, W Liu, Y Wang, et al. Laser additive manufacturing on metal matrix composites: A review. *Chinese Journal of Mechanical Engineering*, 2021, 34(3): 195–210.

[7] Q Mu, L Wang, C K Dunn, et al. Digital light processing 3D printing of conductive complex structures. *Additive Manufacturing*, 2017, 18: 74–83.

[8] Q Mu, C K Dunn, L Wang, et al. Thermal cure effects on electromechanical properties of conductive wires by direct ink write for 4D printing and soft machines. *Smart Materials and Structures*, 2017, 26(4): 045008.

[9] J Persad, S Rocke. A survey of 3d printing technologies as applied to printed electronics. *IEEE Access*, 2022, 10: 27289–27319.

[10] J Ren, Y Zhang, D X Zhao, et al. Strong yet ductile nanolamellar high-entropy alloys by additive manufacturing. *Nature*, 2022, 608: 62–68.

[11] Z Jiang, P Shen, M L Tan, et al. 3D and 4D printable dual cross-linked polymers with high strength and humidity-triggered reversible actuation. *Materials Advances*, 2021, 2: 5124–5134.

[12] J Y Chen, X J Liu, Y J Tian, et al. 3D-printed anisotropic polymer materials for functional applications. *Advanced Materials*, 2021, 34(5): 2102877.

[13] L Y Zhou, J Z Fu, Y He, A review of 3D printing technologies for soft polymer materials. *Advanced Functional Materials*, 2020, 30(28): 2000187.

[14] Z C Guan, L Wang, J Bae. Advances in 4D printing of liquid crystalline elastomers: Materials, techniques, and applications. *Materials Horizons*, 2022, 9: 1825–1849.

[15] E M Palmero, A Bollero. 3D and 4D printing of functional and smart composite materials. *Encyclopedia of Materials: Composites*, 2021, 2: 402–419.

[16] G Liu, Y Zhao, G Wu, et al. Origami and 4D printing of elastomer-derived ceramic structures. *Science Advances*, 2018, 4(8): eaat064.

[17] R P Chaudhary, C Parameswaran, M Idrees, et al. Additive manufacturing of polymer-derived ceramics: Materials, technologies, properties and potential applications. *Progress in Materials Science*, 2022, 128: 100969.

[18] D Menne, L L Silva, M Rotan, et al. Giant functional properties in porous electroceramics through additive manufacturing of capillary suspensions. *ACS Applied Materials & Interfaces*, 2022, 14: 3027–3037.

[19] Y F Zhang, N Zhang, H Hingorani, et al. Soft robots: Fast-response, stiffness-tunable soft actuator by hybrid multimaterial 3D printing. *Advanced Functional Materials*, 2019, 29(15): 1970098.

[20] Y Yan, Z Xiong, Y Hu, et al. Layered manufacturing of tissue engineering scaffolds via multi-nozzle deposition. *Materials Letters*, 2003, 57(18): 2623–2628.

[21] L Geng, W Feng, D W Hutmacher, et al. Direct writing of chitosan scaffolds using a robotic system. *Rapid Prototyping Journal*, 2005, 11(2): 90–97.

[22] D Espalin, J Alberto Ramirez, F Medina, et al. Multi-material, multi–technology FDM: Exploring build process variations. *Rapid Prototyping Journal*, 2014, 20(3): 236–244.

[23] Z Ding, C Yuan, X Peng, et al. Direct 4D printing via active composite materials. *Science Advances*, 2017, 3(4): 1602890.

[24] *3D-Bioplotter Technical Data*, envisionTEC, 2022(9/25). https://etec.desktopmetal.com/

[25] A Parihar, V Pandita, A Kumar, et al. 3D printing: Advancement in biogenerative engineering to combat shortage of organs and bioapplicable materials. *Regenerative Engineering and Translational Medicine*, 2022, 8: 173–199.

[26] H Y Shen, L Pan, Q Jun. Research on large-scale additive manufacturing based on multi-robot collaboration technology. *Additive Manufacturing*, 2019, 30: 100906.

[27] Z Y Zhang, C M Wu, C K Dai, et al. A multi-axis robot-based bioprinting system supporting natural cell function preservation and cardiac tissue fabrication. *Bioactive Materials*, 2022, 18: 138–150.

[28] O Neri, D R Jorge, K Steven, et al. Towards robotic swarm printing. *Architectural Design*, 2014, 84(3): 108–115.

[29] L J Wu, J Q Yang, X W Zhang, et al. Multi manipulator cooperative 3D printing based on Dobot manipulator. *Materials Science and Engineering*, 2018, 382: 042040.

[30] G Hunt, F Mitzalis, T Alhinai, et al. 3D printing with flying robots. *IEEE Int. Conf. on Robotics and Automation*, Hong Kong, China, May 31–June 7, 2014: 4493–4499.

[31] Y Jin, H A Pierson, H Liao. Concurrent fused filament fabrication with multiple extruders. *2017 Institute of Industrial Engineers International Conference. Proceedings*. Institute of Industrial and Systems Engineers (IISE), 2017.

[32] N Fontaine. Modular user-configurable multi-part 3D layering system and hot end assembly: US, 10456992. 2019–10–29[2022-05-13]. https://patents.justia.com/patent/10456992.

[33] M Uzan, I Yakubov. Additive manufacturing device: US, 9011136. 2015-04-21[2022-05-13]. http://www.google.dj/patents/US9011136.

[34] X Zhang, M Li, J H Lim, et al. Large-scale 3D printing by a team of mobile robots. *Automation in Construction*, 2018, 95(11): 98–106.

[35] J Mcpherson, W Zhou. A chunk-based slicer for cooperative 3D printing. *Rapid Prototyping Journal*, 2018, 24(9): 1436-1466.

Li *et al. Chinese Journal of Mechanical Engineering*   (2023) 36:140

Page 20 of 20

[36] N Khani, A Nadernezhad, P Bartolo, et al. Hierarchical and spatial modeling and bio-additive manufacturing of multi-material constructs. *CIRP Annals-Manufacturing Technology*, 2017, 66(1): 229–232.

[37] E B Joyeea, Y Pan. Multi-material additive manufacturing of functional soft robot. *Procedia Manufacturing*, 2019, 34: 566-573.

[38] K Kun. Reconstruction and development of a 3D printer using FDM technology. *Procedia Engineering*, 2016, 149: 203–211.

[39] Y Wei, K H Wang, W Zhang. Design of industrial CT multi-axis positioning system based on PMAC. *Mechanical Engineering & Automation*, 2019, 4: 200–201. (in Chinese)

[40] W Wang, J Chen, C Xiao, et al. Adaptive fuzzy control method of hydrogen fuel cell gas supply system. *Journal of Physics: Conference Series*, 2021, 1983(1): 012051.

[41] F Gan, Z Liu, C Ren, et al. Robot's motion error and online compensation based on force sensor. *Chinese Journal of Mechanical Engineering*, 2007, 20(4): 8–11.